ADVANCED ENERGY MATERIALS
www.advenergymat.de

Examining the Electrochemical Properties of Hybrid Aqueous/Ionic Liquid Solid Polymer Electrolytes through the Lens of Composition-Function Relationships

*Kyle B. Ludwig, Riordan Correll-Brown, Max Freidlin, Mounesha N. Garaga, Sahana Bhattacharyya, Patricia M. Gonzales, Arthur V. Cresce, Steven Greenbaum, Chunsheng Wang, and Peter Kofinas**

Solid polymer electrolytes (SPEs) have the potential to meet evolving Li-ion battery demands, but for these electrolytes to satisfy growing power and energy density requirements, both transport properties and electrochemical stability must be improved. Unfortunately, improvement in one of these properties often comes at the expense of the other. To this end, a "hybrid aqueous/ionic liquid" SPE (HAILSPE) which incorporates triethylsulfonium-TFSI ($S_{2,2,2}$) or *N*-methyl-*N*-propylpyrrolidinium-TFSI ($Pyr_{1,3}$) ionic liquid (IL) alongside H_2O and LiTFSI salt to simultaneously improve transport and electrochemical stability is studied. This work focuses on the impact of HAILSPE composition on electrochemical performance. Analysis shows that an increase in LiTFSI content results in decreased ionic mobility, while increasing IL and water content can offset its impact. pfg-NMR results reveal that preferential lithium-ion transport is present in HAILSPE systems. Higher IL concentrations are correlated with an increased degree of passivation against H_2O reduction. Compared to the $Pyr_{1,3}$ systems, the $S_{2,2,2}$ systems exhibit a stronger degree of passivation due to the formation of a multicomponent interphase layer, including LiF, Li_2CO_3, Li_2S, and Li_3N. The results herein demonstrate the superior electrochemical stability of the $S_{2,2,2}$ systems compared to $Pyr_{1,3}$ and provide a path toward further enhancement of HAILSPE performance via composition optimization.

1. Introduction

The rise of lithium-ion batteries (LIBs) to ubiquity over the last 30 years has been due, in part, to their long cycle lives, high charge–discharge rates, high specific energy (≈150 Wh kg^{-1}), and low cost.[1–5] Decades of research and technical advancements have been fueled by applications that demand high power density (power tools, rapid charging) or high energy density (portable electronics, electric vehicles).[6–8] Despite the progress of commercial LIBs, these demands are gradually approaching the theoretical limits of current materials and are outpacing the discovery of new ones.[9,10] At the same time, appeals to improve the safety of LIBs have become prominent. To address these concerns, strategies must be developed to determine safer materials that ensure compatibility with both high power density and high energy density applications.[11,12]

Solid polymer electrolytes (SPEs) are safer materials that can improve the

K. B. Ludwig, R. Correll-Brown, M. Freidlin, S. Bhattacharyya, C. Wang, P. Kofinas
Department of Chemical & Biomolecular Engineering
University of Maryland
4418 Stadium Dr, College Park, MD 20740, USA
E-mail: kofinas@umd.edu

M. N. Garaga, S. Greenbaum
Department of Physics & Astronomy
Hunter College of the City University of New York
695 Park Ave, New York, NY 10065, USA

P. M. Gonzales
Department of Materials Science & Engineering
University of Maryland
4418 Stadium Dr, College Park, MD 20740, USA

A. V. Cresce
Battery Science Branch, Energy Science Division, Sensors and Electron Devices Directorate
DEVCOM US Army Research Laboratory
2800 Powder Mill Rd, Adelphi, MD 20783, USA

The ORCID identification number(s) for the author(s) of this article can be found under https://doi.org/10.1002/aenm.202301428

DOI: 10.1002/aenm.202301428

efficacy of LIBs. They represent an attractive alternative to the flammable organic liquid electrolytes commonly used in commercial batteries because they are nonflammable, lightweight, and can prevent leaking of toxic solvents and salts.[13] However, in high power density applications, which rely on fast ionic transport and charge transfer, SPEs fail to meet the demand as their ionic conductivity and lithium-ion (Li^+) transport number are generally limited (10^4–10^6 S cm^{-1}, <0.40) due to polymer crystallinity and/or high glass-transition temperatures (T_g).[14] To improve the power density of SPEs, researchers have focused on improving ionic transport by adding plasticizers such as ceramic particles, ionic liquids (ILs) and even water to the electrolyte system to suppress polymer crystallinity and imbue chain mobility.[15–17] In polymer-in-salt electrolytes, the inclusion of ionic liquids can also facilitate charge transfer in high power density applications by improving interfacial contact at the electrode/electrolyte interface through the development of robust solid electrolyte interphases (SEIs).[13,18–20]

For high energy density applications (E = V × Capacity), SPEs can meet the demand through strategies that extend the electrochemical stability window (ESW). This unlocks a wider range of electrode materials, such that the voltage output or capacity can be rationally designed. In the case of aqueous SPEs (ASPEs) – a noteworthy modification to SPEs that improves transport and ensures safety by using water as a solvent and plasticizer – this is realized through contemporaneous improvement at both the anodic and cathodic limits.[21] By switching from the traditional poly(ethylene oxide) (PEO) support to polyacrylonitrile (PAN), the thermodynamic instability at 4 V versus Li/Li^+ due to oxidation of the electron-rich ether oxygens in PEO-based SPEs can be avoided.[22,23] PAN-based SPEs have shown enhanced anodic limits upward of ≈5.5 V versus Li/Li^+.[24,25] At the cathodic limit, minimizing the activity of water assists in lowering its onset reduction potential that allows for anion-derived passivation and SEI formation. This can be achieved through the "water-in-salt" electrolyte (WiSE) strategy of superconcentrated systems utilizing bis(trifluoromethylsulfonyl)imide anion ($[TFSI]^-$)-based salts.[26–28]

Practically, the optimization of power density and energy density come as a tradeoff. As seen in a new class of "hybrid aqueous/nonaqueous" electrolytes (HANEs), although the inclusion of a nonaqueous component can extend the ESW and boost the energy density of the system, it often leads to significant drops in ionic conductivity. For example, the inclusion of dimethyl carbonate resulted in further reduction of the cathodic limit – from 1.9 V versus Li/Li^+ in the groundbreaking WiSE system to 1.0 V versus Li/Li^+ in the subsequent HANE system – at the cost of reducing the ionic conductivity by nearly half.[26,29] In recent work, we demonstrated that the incorporation of triethylsulfonium-TFSI ($S_{2,2,2}$) or *N*-methyl-*N*-propylpyrrolidinium-TFSI ($Pyr_{1,3}$) ILs (Figure S1, Supporting Information) as the nonaqueous components of "hybrid aqueous/ionic liquid" SPEs (HAILSPEs) can overcome this conductivity challenge. These electrolyte systems exhibited a remarkable improvement in transport properties compared to their predecessors due to the reduction in apparent activation energy and nearly complete decoupling of ionic transport from polymer chain mobility.[30] We also demonstrated stable and complete growth of a passivating layer that was tuned by changing the IL. The sulfur-based $S_{2,2,2}$ cation was chosen based on previous studies of a nonaqueous ionic liquid SPE (ILSPE) which concluded that the inclusion of the ionic liquid resulted in strong passivating behavior and interfacial stability with lithium metal.[17] The nitrogen-based $Pyr_{1,3}$ cation was chosen as an additional promising cation based on numerous reports of its stable electrochemical reduction products, such as Li_3N, and its ability to contribute to LiF formation in the SEI when paired with the $[TFSI]^-$ in lithiated systems.[30] After this precursory work, which primarily explored the impact different ionic liquid types, we sought to better understand how the composition-function relationships describe the electrochemical properties in these systems.

In this work, we further investigated HAILSPE systems, expanding the design space to include more than 30 electrolyte compositions with varying molar ratios of PAN, water, ionic liquid, and lithium TFSI (LiTFSI) salt. Extensive analysis of the transport properties found that a continued increase in the LiTFSI content resulted in a significant drop off in ionic conductivity, despite the simultaneous increase in H_2O, a component that is known to improve mobility. As increasing LiTFSI concentration is a core strategy employed in most aqueous electrolytes to widen the ESW, this effect was offset by incorporation of additional IL. Pulsed-field gradient NMR (pfg-NMR) results corroborated these findings and further cemented that the influence of LiTFSI on transport properties supersedes that of H_2O. Nevertheless, all HAILSPE systems demonstrated preferential Li^+ transport, as evidenced by transport numbers of 0.64–0.80, depending on the composition. Linear sweep voltammetry (LSV) and cyclic voltammetry (CV) were used to assess the ESW and passivation behavior of several HAILSPEs. Generally wide windows were observed, depending on the composition, with $S_{2,2,2}$ electrolytes demonstrating greater electrochemical stability than their $Pyr_{1,3}$ counterparts. Furthermore, increasing the amount of IL was shown to assist with passivation against water reduction, even when the H_2O content increased, with the $S_{2,2,2}$ electrolytes exhibiting superior passivation. X-ray photoelectron spectroscopy (XPS) analysis showed that this may be attributed to the formation of more lithium fluoride (LiF) and lithium carbonate (Li_2CO_3) in $S_{2,2,2}$ systems over $Pyr_{1,3}$ systems. Despite the benefits observed for the $S_{2,2,2}$ electrolytes, cycling of analogous liquid "hybrid aqueous/ionic liquid" electrolytes (HAILEs) in $Mo_6S_8/LiMn_2O_4$ full cells demonstrated nearly identical performance from both. These cells demonstrated an open circuit voltage (OCV) of ≈2.3 V and were cycled at 1 C to 100 cycles with ≥99.0% coulombic efficiency.

2. Results and Discussion

To better understand the ways in which composition influences the electrochemical properties of HAILSPEs, a variety of electrolyte compositions and characterized to elucidate the effect of each component. Tables S1–S7, Supporting Information give the final compositions, in relative molar amounts, for all electrolyte systems used in this work; 3.27–13.57 parts PAN, 6.94–57.30 parts H_2O, 0–4 parts ionic liquid, and 3.03–17.06 parts LiTFSI. The relative molar amount of PAN is based on the monomer repeat unit (53.06 g mol^{-1}) to ensure the analyses presented in this work form design goals that are independent of the polymer molecular weight and clarify the influence of water, IL, and

LiTFSI on electrolyte properties. The compositions were carefully selected based on a posteriori knowledge to cover a wide range of polymer, water, ionic liquid, and salt contents that yielded well-mixed, homogeneous films which were not phase separated. Two versions of electrolytes H1–H18 and NMR1–NMR8 were made using either $S_{2,2,2}$ or $Pyr_{1,3}$, except for "NMR3" which contained no ionic liquid. Although the electrolytes were designed in groups to elucidate the effect of a single component by keeping all others constant, the hygroscopicity of the systems caused additional water absorption during processing in ambient conditions and often resulted in electrolytes within the same group having differing water contents. However, absorbed water was accounted for via thermogravimetric analysis (TGA) measurements post-processing and the analyses presented in this work reflect the complexity of these quaternary systems.

2.1. Impedance and Ionic Transport

2.1.1. EIS and mDSC

The room-temperature (25 °C) electrochemical impedance spectroscopy (EIS) response of HAILSPE systems $S_{2,2,2}/Pyr_{1,3}$ H1–H18 and $Pyr_{1,3}$ H19–H24 were measured to assess ionic mobility as a function of composition. Ionic conductivity, in units of mS cm^{-1}, was calculated from

$$\sigma = 1000\frac{t}{R \times A} \tag{1}$$

where t (cm) and A (cm^2) are the thickness and area, respectively, of the electrolyte defined by the polytetrafluoroethylene (PTFE) spacer, and R is the ohmic resistance. R values were extracted from the impedance response following a detailed procedure outlined elsewhere.[30] Impedance responses varied based on HAILSPE composition and fell into two categories based on their Nyquist plot: those that showed a capacitive effect and those that did not. For the electrolytes that did show capacitance, an equivalent circuit model was used that contained a resistor (R1) in series with a second resistor (R2) that is in parallel with a capacitor. To account for the non-ideal behavior seen in the Nyquist plots, a constant phase element was used in place of the ideal capacitor. In these systems, R1 is indicative of the bulk electrolyte resistance to ionic motion while R2 is indicative of the double layer resistance to ionic motion at the electrode interface. Therefore, the sum of R1 and R2 was used to find R for Equation (1). For the electrolytes that did not show capacitance, a simple equivalent circuit model for a pure ionic conductor, which consists of a single resistor, was used to find R from the intercept of the data at high frequencies.

Figure 1 shows the room-temperature ionic conductivity data for $S_{2,2,2}$ H1–H14, $Pyr_{1,3}$ H1–H14, and $Pyr_{1,3}$ H19–H22, which all contain 1 part ionic liquid, as a function of PAN, H_2O, and LiTFSI composition. Values are indicated by color, with cooler colors (blue) representing low values and warmer colors (red) representing high values. For both $S_{2,2,2}$ and $Pyr_{1,3}$ electrolytes, Figure 1A,B clearly show that increasing the relative amount of PAN or LiTFSI in the electrolyte significantly reduces ionic conductivity. Yet, the impact of water is less clear, as a maximum ionic conductivity value is observed only at moderate water concentrations. The ovals in Figure 1 highlight two noteworthy regions for each set of electrolytes. In the first region, between 10 and 30 parts H_2O, the ionic conductivity values for both $S_{2,2,2}$ and $Pyr_{1,3}$ systems are >5 mS cm^{-1} with less than 8 parts LiTFSI in Figure 1C,D, respectively. In the second region, the water content is doubled to 30–60 parts, but the ionic conductivity values decrease significantly by ≈68% to 2.26 mS cm^{-1} for $S_{2,2,2}$ and by ≈85% to 1.25 mS cm^{-1} for $Pyr_{1,3}$ at the highest amount of water (H14). However, compositions with >30 parts H_2O also correspond to the electrolyte systems with the highest LiTFSI content between 12 and 16 parts. To clarify these trends, a more heuristic description of the impacts of composition on ionic conductivity in both $S_{2,2,2}$ and $Pyr_{1,3}$ electrolytes is presented in **Figure 2**.

In Figure 2A and Figure 2E, both $S_{2,2,2}$ and $Pyr_{1,3}$ systems show a significant increase in ionic conductivity when H_2O is increased and the ionic liquid and LiTFSI contents are held constant. This finding is in agreement with several previous works, which observed that ionic mobility is strongly positively correlated to water concentration.[17,30,31] However, these trends are limited to water contents <30 parts when LiTFSI content does not also increase. As discussed above and shown in Figure 2C,G, increasing LiTFSI content, even marginally, results in a decrease in ionic conductivity because LiTFSI can aggregate and crystallize at high concentrations, ultimately impeding ionic motion. A similar trend is observed for PAN, in Figure 2D,H; increasing the amount of polymer in the system can increase the degree of crystallinity, resulting in lower ionic conductivity due to the lack of segmental motion.[32] The decoupling of ionic transport and polymer chain mobility has been observed in PAN-based electrolytes such that polymer segmental motion is not a major contributor to ionic motion. Electrolyte crystallinity imparted by the polymer matrix – or LiTFSI aggregates – also impedes the movement of free Li^+ and Li^+ associated with plasticizer molecules, which are the major contributors to ionic conductivity in these electrolytes.[30,33–35] As such, the decrease of ionic conductivity with the increase of LiTFSI agrees with the results seen in Figure 1, suggesting that the influence of salt on ionic mobility supersedes that of water in regions of the design space where the relative LiTFSI content is >8 parts (H12–H15, Tables S1, S2, Supporting Information).

In Figure 1, the electrolyte compositions >30 parts H_2O (H12–H14) were extraneous systems that did not fit the general categories of Tables S1 and S2, Supporting Information, because PAN, H_2O, and ionic liquid contents all changed. To more closely investigate the transition in ionic conductivity at high LiTFSI content, and to remove any effect from PAN, electrolytes H19–H21 were designed and further studied in **Figure 3**. Since $Pyr_{1,3}$ H14 showed the largest reduction in ionic conductivity (≈85%), only $Pyr_{1,3}$ H19–H21 electrolytes were synthesized (Table , Supporting Information). Although these compositions were designed to have the same overall water content and were handled in an environment with a controlled humidity, the hygroscopicity of each electrolyte was different due to their varying salt contents. This led to a large degree of water absorption in the system with the most salt in Figure 3A. At 15 parts LiTFSI, $Pyr_{1,3}$ H21 (blue) had the lowest ionic conductivity of the three systems (0.18 mS cm^{-1}), despite having the highest water content. Conversely, $Pyr_{1,3}$ H19 (pink) had the least amount of salt – and water – but displayed the highest ionic conductivity (0.97 mS cm^{-1}). A one-way ANOVA on

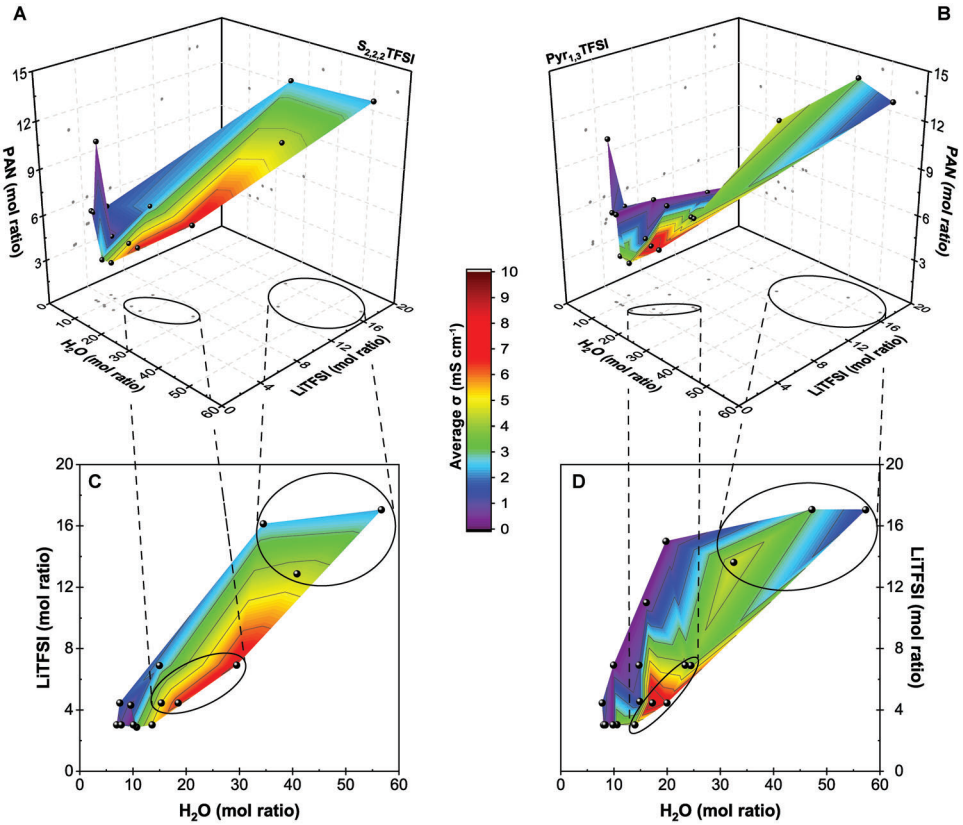

Figure 1. Room-temperature (25 °C) ionic conductivity as a function of PAN, H_2O, and LiTFSI content for A) $S_{2,2,2}$ H1–H14 and B) $Pyr_{1,3}$ H1–H14, H19–H22. The ionic conductivity values as a function of just H_2O and LiTFSI are also given for C) $S_{2,2,2}$ and D) $Pyr_{1,3}$. Conductivity is indicated by color, with cooler colors representing low values and warmer colors representing high values. Ovals are used to highlight two notable regions for each set of electrolytes: one where compositions yield high ionic conductivity (>5 mS cm^{-1}) and one where compositions yield significantly reduced ionic conductivity (<5 mS cm^{-1}) despite high water content. All electrolyte compositions are given in Tables S1–S3, Supporting Information.

the mean ionic conductivities of $Pyr_{1,3}$ H19–H21 at a 95% confidence interval (Figure S2A, Supporting Information) showed that H19 and H21 exhibit a statistically significant conductivity difference with a *p*-value of 0.0045, while H19 and H20 also exhibit a statistically significant conductivity difference with a *p*-value of 0.0393. Due to the large variation amongst the H20 samples – likely caused by minor fluctuations in water content despite being processed at the same time – the one-way ANOVA found the difference between H20 and H21 was not statistically significant ($p = 0.3592$). However, the general trend of the HAILSPE systems investigated in Figure 3A agrees with the trends observed in the HAILSPE systems investigated in Figures 1 and 2.

To further understand the results of Figure 3A, the thermal properties of the three electrolytes were investigated via modulated differential scanning calorimetry (mDSC); their thermograms are shown in Figure 3B. The resulting $Pyr_{1,3}$ H19 electrolyte (pink) exhibited a solid-liquid melting transition, T_m, at −1.61 °C. $Pyr_{1,3}$ H20 (green), which had the next highest ionic conductivity ≈0.45 mS cm^{-1}, exhibited two solid-solid rearrangements ($T_{s\text{-}s}$), at 0.32 and 19.43 °C, before ultimately exhibiting a T_m at 30.49 °C. $Pyr_{1,3}$ H21 (blue), which had the lowest ionic conductivity, exhibited a $T_{s\text{-}s}$ at 5.77 °C and a T_m at 43.07 °C. The formation of multiple endothermic peaks upon heating for $Pyr_{1,3}$ H20 and $Pyr_{1,3}$ H21 is attributed to the presence of "excess" water and/or ionic liquid which do not significantly interact with the other components.[18] $Pyr_{1,3}$ H20 and $Pyr_{1,3}$ H21 also exhibit melting temperatures significantly greater than that of $Pyr_{1,3}$ H19 and the operating temperature of 25 °C, with an increase in the breadth and intensity of the melting transition. The latent heat for $Pyr_{1,3}$ H20 and $Pyr_{1,3}$ H21 – found from the area under the curve – is 12.71 and 10.05 J g^{-1}, respectively. Compared to the latent heat of 0.88 J g^{-1} for $Pyr_{1,3}$ H19, this suggests a meaningful increase in the degree of crystallinity for these two systems. Thus, the broader melting transitions in $Pyr_{1,3}$ H20 and $Pyr_{1,3}$ H21 are likely the result of a wider distribution of crystal sizes.[36] Furthermore, while many different factors affect T_m, the increase in T_m for $Pyr_{1,3}$ H20 and $Pyr_{1,3}$ H21 is likely due to this increase in crystallinity, since crystalline lamellae exhibit strong intermolecular forces that severely restrict chain flexibility and increase latent heat. These findings agree with the conductivity values reported in Figure 3A, as crystalline structures would impose effective restrictions on the mobility of ions, reducing ionic conductivity.[37]

While Figure 3C demonstrates that ionic conductivity increases with increasing relative ionic liquid content up to 1 part, Figure 2B,F shows that beyond this point, further increasing the amount of IL in the system begins to decrease ionic conductivity; from 2.29 to 1.44 mS cm^{-1} when increasing the relative amount of $S_{2,2,2}$ to 3 parts from 1, and from 3.56 to 1.89 mS

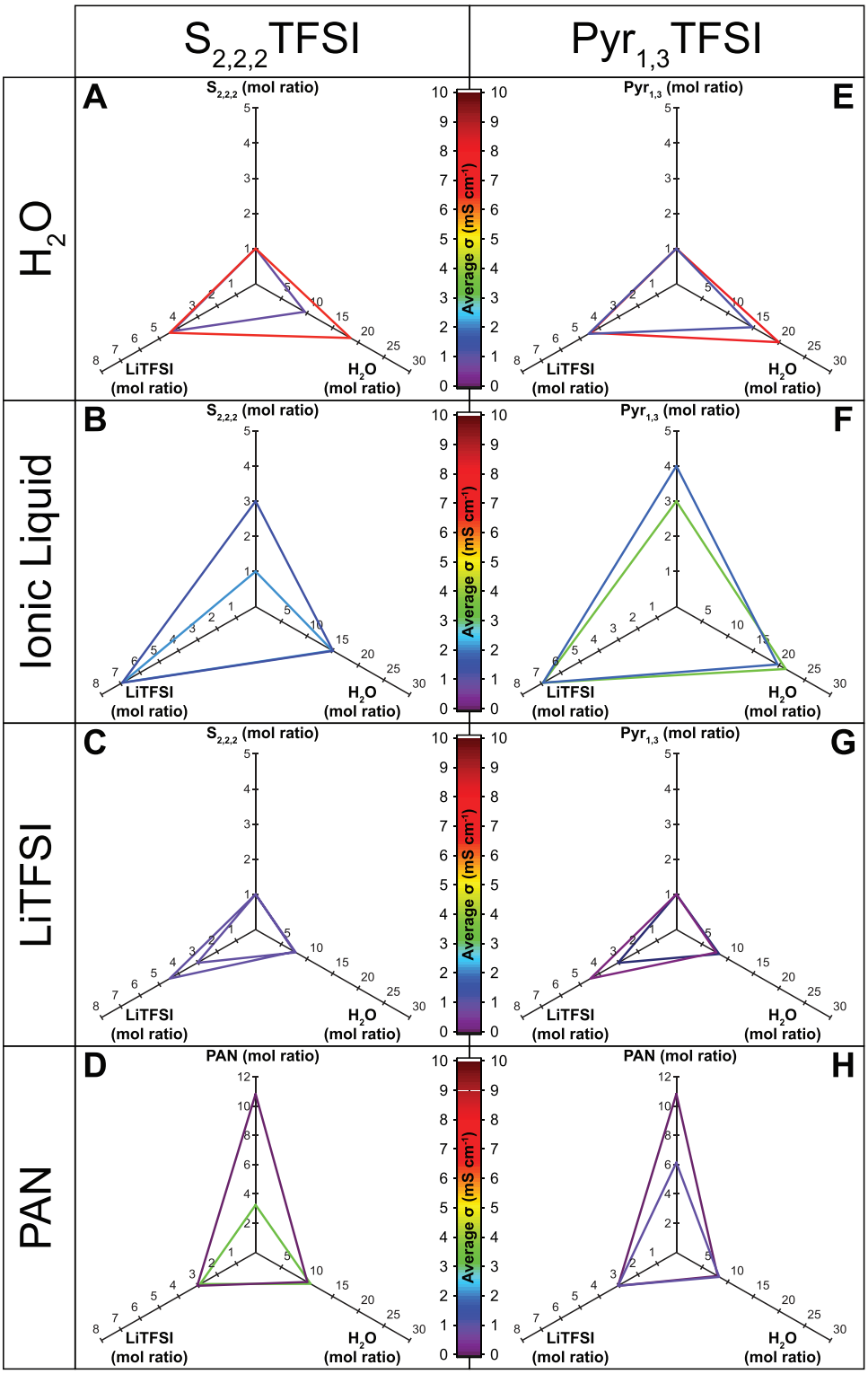

Figure 2. Radar plots displaying representative trends in room-temperature (25 °C) ionic conductivity based on altering H_2O, ionic liquid, LiTFSI, and PAN composition for A–D) $S_{2,2,2}$ and E–H) $Pyr_{1,3}$ electrolyte systems. Conductivity is indicated by color based on the provided scale bars, with cooler colors representing low values and warmer colors representing high values. For H_2O, ionic liquid, and LiTFSI, the relative PAN molar ratio was held constant at 6.14. For PAN, the relative ionic liquid molar ratio was held constant at 1.

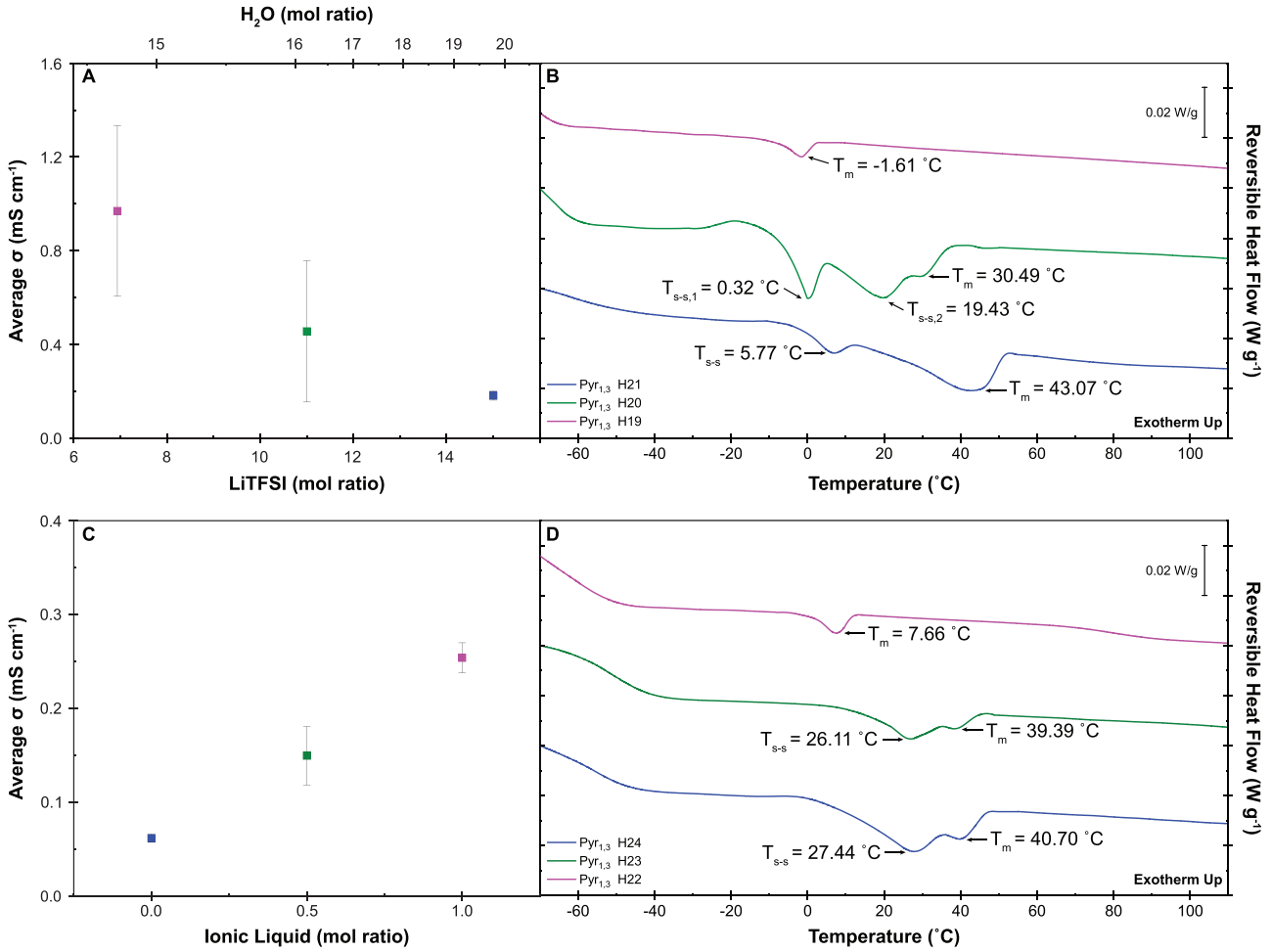

Figure 3. Ionic conductivity as a function of relative composition and associated mDSC thermograms for corresponding electrolyte systems (blue, green, pink) for A,B) LiTFSI and H_2O ($Pyr_{1,3}$ H19–H21) and C,D) ionic liquid ($Pyr_{1,3}$ H22–H24). Relevant thermal transitions, such as solid-solid and melting, and their associated temperatures are labeled. All electrolyte compositions are given in Table S3, Supporting Information.

cm^{-1} when increasing the relative amount of $Pyr_{1,3}$ from 3 parts to 4. Phase separation of the ionic liquid from the bulk electrolyte may be the cause of these drops in conductivity, which was visually observed for systems whose relative ionic liquid content was >2 parts. To this end, the importance of ionic liquid on transport properties below the observed limit of phase separation was also more closely investigated with electrolytes $Pyr_{1,3}$ H22, $Pyr_{1,3}$ H23, and H24 (no ionic liquid) in Figure 3C. As the relative LiTFSI content in these electrolytes was held constant, the variation in water content was relatively constant, ranging between 8.82 and 10.75 parts (Table S3, Supporting Information). With 1 part ionic liquid, $Pyr_{1,3}$ H22 (pink) had the highest room-temperature ionic conductivity of 0.25 mS cm^{-1}. When the ionic liquid content was halved in $Pyr_{1,3}$ H23 (green) the conductivity decreased to 0.15 mS cm^{-1}, and when the ionic liquid was completely removed from the electrolyte in H24 the ionic conductivity decreased even further to 0.06 mS cm^{-1}. The room-temperature conductivity values of these electrolyte systems are consistent with Figure 1 and other systems with <10 parts water. A one-way ANOVA of the mean ionic conductivities at a 95% confidence interval was also performed for $Pyr_{1,3}$ H22, $Pyr_{1,3}$ H23, and H24. In this case, because the water contents were relatively constant, the differences of all possible combinations were found to be statistically significant with p-values <0.001 (Figure S2B, Supporting Information).

The results of Figure 3C clearly indicate that the inclusion of ionic liquid, to an extent, can promote ionic mobility; Figure 3D further explores this result through mDSC. The $Pyr_{1,3}$ H22 system (pink), which has 1 part ionic liquid, exhibited a T_m at 7.66 °C with a latent heat of 1.01 J g^{-1}. As the amount of ionic liquid in the electrolytes was decreased, a positive shift in T_m and an increase in latent heat was observed. $Pyr_{1,3}$ H23 (green, 0.5 parts ionic liquid) exhibited a T_m at 39.39 °C with a latent heat of 4.10 J g^{-1} and H24 (blue, 0 parts ionic liquid) exhibited a T_m at 40.70 °C with a latent heat of 9.11 J g^{-1}. $Pyr_{1,3}$ H23 and H24 also exhibited a single $T_{s\text{-}s}$ at 26.11 and 27.44 °C, respectively. As with the increase in LiTFSI content observed in Figure 3B, the decrease in ionic liquid content yielded electrolytes that exhibited an increase in the breadth and amplitude of melting transitions. This indicates an increased degree of crystallinity, which is correlated with the decrease in ionic conductivity shown in Figure 3C. Thus, the results of Figure 3D suggest that ionic liquid is an effective plasti-

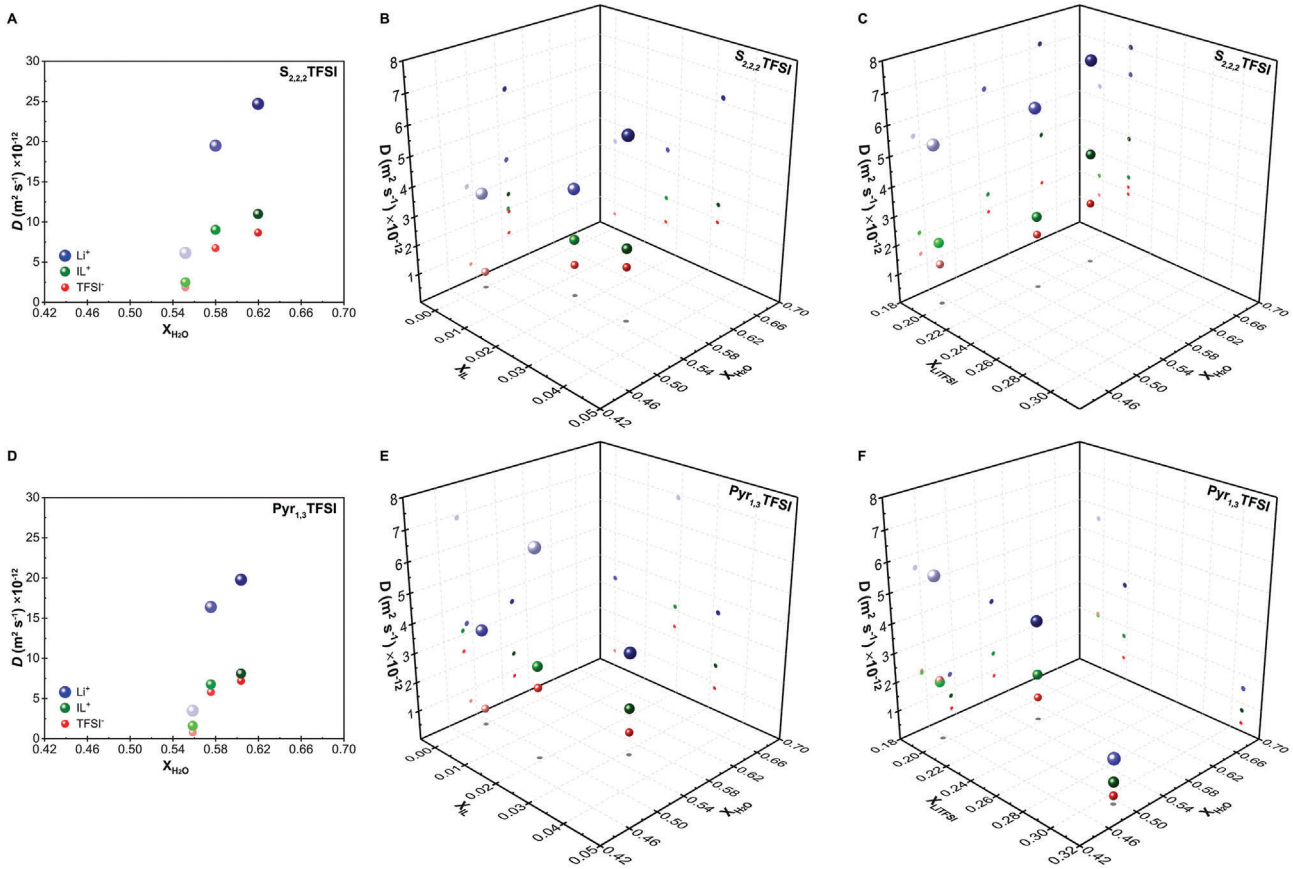

Figure 4. pfg-NMR results highlighting the influence of H_2O ("group 3"), ionic liquid ("group 1"), and LiTFSI ("group 2") concentration on diffusion coefficients of Li^+, IL^+, and $[TFSI]^-$ for A–C) $S_{2,2,2}$ and D–F) $Pyr_{1,3}$ electrolyte systems. (A/D) represent group 3, (B/E) represent group 1, and (C/F) represent group 2. All electrolyte compositions are given in Tables S4–S7, Supporting Information.

cizer that assists in reducing crystallinity and lifting restrictions on ionic mobility, resulting in an increase in ionic conductivity.

2.1.2. pfg-NMR and Lineshape Analysis

Ionic transport in HAILSPEs was also investigated with pfg-NMR. Much like compositions H1–H18, systems were carefully designed and categorized into three main groups, each focusing on how ionic liquid, LiTFSI, or water influences transport. Tables S4–S7, Supporting Information, give the relevant compositions for the different systems (NMR1–7) for both $S_{2,2,2}$ and $Pyr_{1,3}$. From pfg-NMR measurements, diffusion coefficients for H_2O (^1H), Li^+ (^7Li), ionic liquid cations (IL^+) ($[S_{2,2,2}]^+/[Pyr_{1,3}]^+$; ^1H), and $[TFSI]^-$ (^{19}F) were calculated and plotted in **Figure 4**. Each plot within Figure 4 focuses on one of three groups in Tables S4–S7, Supporting Information, with Figure 4A–C corresponding to $S_{2,2,2}$ electrolytes and Figure 4D–F corresponding to $Pyr_{1,3}$ electrolytes. From Figure 4, it is immediately clear that the diffusion coefficient of Li^+ (D_{Li^+}) is greater than that of IL^+ (D_{IL^+}) or $[TFSI]^-$ (D_{TFSI^-}), indicating preferential cation transport. In fact, the diffusion coefficients follow the same order for all electrolytes, regardless of changes to composition: D_{Li^+} (blue) > D_{IL^+} (green) > D_{TFSI^-} (red). When only water content is changed, Figure 4A,D ("group 3") suggest that transport is increased for all available ions in both $S_{2,2,2}$ and $Pyr_{1,3}$ systems, respectively. Curiously, the diffusion coefficients increase dramatically, in both systems, when $X_{H_2O} > 0.55$.

While efforts were made to keep water content as constant as possible, the hygroscopic nature of the electrolyte systems resulted in water content changing when either ionic liquid or LiTFSI content was also changed. As a result, Figure 4B,E ("group 1") and Figure 4C,F ("group 2") present the results as a function of both IL and H_2O or LiTFSI and H_2O content. For $S_{2,2,2}$ electrolyte systems, increasing ionic liquid concentration in Figure 4B clearly leads to increased Li^+ ionic mobility, as D_{Li^+} increases from $\approx 3.75 \times 10^{-12}$ to 6.16×10^{-12} $m^2\ s^{-1}$ when the ionic liquid content is doubled at the same water concentration ($X_{H_2O} = 0.55$). Similarly, for $Pyr_{1,3}$ electrolyte systems, increasing ionic liquid content in Figure 4E from 0 (NMR3) to 0.5 parts ($Pyr_{1,3}$ NMR2) resulted in an increase in D_{Li^+} from 3.34×10^{-12} to 6.90×10^{-12} $m^2\ s^{-1}$ at $X_{H_2O} = 0.49$. Interestingly, further increasing the amount of ionic liquid from 0.5 parts to 1 part ($Pyr_{1,3}$ NMR1) subsequently decreased D_{Li^+} to 3.50×10^{-12} $m^2\ s^{-1}$, which is similar to that of NMR3. This is likely due to an overestimation of the water content caused by minor changes between the NMR1 sample that was measured with pfg-NMR and the sample that was measured with TGA to calculate the final water amount. The

H_2O diffusion coefficient for $Pyr_{1,3}$ NMR1 (1.73×10^{-11} m^2 s^{-1}) corroborates this claim, as it is consistent with that of NMR3 (1.69×10^{-11} m^2 s^{-1}) which only has 12.67 parts H_2O.

The influence of LiTFSI content on ionic transport is presented in Figure 4C for $S_{2,2,2}$ electrolytes (NMR1, 4, and 5). The results do not readily show an obvious trend as the salt concentrations are relatively constant. The magnitude of D_{Li^+} does increase – from 6.16×10^{-12} to 7.08×10^{-12} m^2 s^{-1} – with a slight increase in salt concentration from $S_{2,2,2}$ NMR5 ($X_{LiTFSI} = 0.18$) to $S_{2,2,2}$ NMR1 ($X_{LiTFSI} = 0.22$), however X_{H_2O} also increases; this makes it difficult to determine the influence of LiTFSI. When the water concentration is increased at a constant LiTFSI concentration ($X_{LiTFSI} = 0.22$), all three diffusion coefficients increase from $S_{2,2,2}$ NMR1 to $S_{2,2,2}$ NMR2, which is in general agreement with Figures 1 and 2 as well as prior work.[17,30] For the $Pyr_{1,3}$ electrolytes, the influence of LiTFSI concentration on ionic mobility is more obvious in Figure 4F as the diffusion coefficients from $Pyr_{1,3}$ NMR5 ($X_{LiTFSI} = 0.20$) significantly decrease to $Pyr_{1,3}$ NMR4 ($X_{LiTFSI} = 0.31$) when the salt concentration is increased by more than 50%. Despite X_{H_2O} also increasing – from 0.46 to 0.49 – D_{Li^+} still decreases ≈73%, although the change in salt concentration exceeds that of water. If the salt concentration is held relatively constant, however, and X_{H_2O} is significantly increased from 0.46 ($Pyr_{1,3}$ NMR5) to 0.56 ($Pyr_{1,3}$ NMR1; $X_{LiTFSI} = 0.22$), then D_{Li^+} decreases by ≈37%. This supports the claim made above that the influence of salt on ionic mobility supersedes that of water.

Regardless of the composition, all $S_{2,2,2}$ and $Pyr_{1,3}$ electrolytes displayed a majority contribution to ionic conductivity from the movement of Li^+, as shown by the transport number, t_{Li^+}. While in non-aqueous systems this is readily measured using the Bruce-Vincent method, this technique requires a lithium metal reference electrode that is not compatible with our HAILSPEs. Instead, the pfg-NMR results were used to calculate the transport number using

$$t_{Li^+} = \frac{c_{Li^+} \times D_{Li^+}}{\left(c_{Li^+} \times D_{Li^+}\right) + \left(c_{TFSI^-} \times D_{TFSI^-}\right) + \left(c_{IL^+} \times D_{IL^+}\right)} \quad (2)$$

where c_{Li^+}, c_{TFSI^-}, and c_{IL^+} are the concentrations of Li^+, $[TFSI]^-$, and ionic liquid cation ($[S_{2,2,2}]^+/[Pyr_{1,3}]^+$), respectively, in units of mol m^{-3}. The values of t_{Li^+} (Tables S4 and S6, Supporting Information) agree with past work, showing a decrease with additional water content because the concentration of ions decrease.[30] The results also shed new light on t_{Li^+} decreasing with additional ionic liquid and increasing with additional LiTFSI.

As shown in Figure 3B, the mDSC results of $Pyr_{1,3}$ H20 and $Pyr_{1,3}$ H21, which showed multiple endothermic peaks upon heating, suggest various degrees of interaction among the components. These interactions, or lack thereof, can have significant implications. In the context of concentrated solid phase aqueous polymer electrolytes, frequent Li^+–H_2O interactions lead to new domains that facilitate facile ionic transport through the polymer matrix with a high degree of specificity.[17,30] Consequently, this can be limiting to the overall electrochemical stability of the system as lithium ions shuttle H_2O to the electrode surfaces during charging and discharging, causing water reduction and oxidation. Furthermore, non-interacting, or "free," water is also able to diffuse to electrode surfaces. Therefore, a common strategy employed is to limit the overall activity of free, unbound H_2O by increasing the concentration of additional species that force it to interact with less mobile moieties.[26,31,38–41] In the context of concentrated liquid phase aqueous electrolytes – such as the WiSE or HANE – this is beneficial as it allows Li^+–$[TFSI]^-$ interactions to prevail, which leads to anion-derived SEI formation from lithium ions shuttling the anions during charging and discharge.[26,27,29,38,41] To this end, the degree of strongly interacting ("bound") and weakly interacting ("weakly bound") H_2O in HAILSPE systems was investigated.

NMR is a powerful tool for investigating water interactions because spectra are typically sensitive to complex formations and structures, even if interactions are weak.[42] In the absence of interactions, the unbound state has a characteristic, or resonant, frequency of precession. When the unbound state associates with another species, this new interaction alters the local environment causing a shift in this resonant frequency. As such, changes in interactions result in differing spectra depending on several factors, including the degree of interaction, the difference in resonant frequency between the bound (ω_b) and weakly bound (ω_{wb}) states, $\Delta\omega = \omega_{wb} - \omega_b$, and the rate of exchange between bound and weakly bound states, k_{ex}. If $k_{ex} >> \Delta\omega$, then the exchange between states is fast and interactions are observed as a single species-averaged peak with a shifted resonant frequency somewhere between ω_b and ω_{wb}, based on the degree of interaction. However, if $k_{ex} << \Delta\omega$, then the exchange between states is slow and interactions are observed as a change in the relative intensity of the peaks at ω_b and ω_{wb}, based on the degree of interaction. Finally, if $k_{ex} \approx \Delta\omega$, then the exchange between states occurs at similar time lengths as the resonant frequencies of the two states and interactions are observed as a change in the breadth of the peak (broadening) at the resonant frequency.[42–44] Some complex systems may observe all three scenarios. Therefore, to both qualitatively and quantitatively assess the degree of bound and unbound water, a lineshape analysis (LSA) derived from the obtained ^{1}H NMR spectra was conducted.

Figure 5 outlines the LSA for $S_{2,2,2}$ and $Pyr_{1,3}$ NMR1, 6, and 7 ("group 3") where only the relative water content was changed. Qualitatively, Figure 5A,D – which show the measured spectra for $S_{2,2,2}$ and $Pyr_{1,3}$, respectively – suggest that the HAILSPE systems investigated exhibit a low-to-intermediate k_{ex}, evidenced from the peak broadening and differences in amplitude; while chemical shifts did occur, they are not as significant. The amplitude, A, and position, x_o, of the primary peak observed in the deconvoluted spectra (Figure S3, Supporting Information), which is attributed to water and its various states of interaction, were easily extracted from the spectral data (Tables S5 and S7, Supporting Information) for analysis. To quantify the relative peak broadening, the full width at half maximum (FWHM) was calculated of these primary peaks, assuming a Lorentzian lineshape, by

$$FWHM\ (A, x, y) = \sqrt{\frac{4y\left(x_o - x\right)^2}{A - y}} \quad (3)$$

where x and y are an arbitrary pair of frequency and intensity data within ±0.10 ppm of x_o. For the $S_{2,2,2}$ electrolytes in Figure 5A, both amplitude and FWHM correlated strongly with water concentration displaying R^2 values of 0.94 and 0.95, respectively (Figure S4, Supporting Information); as the amount

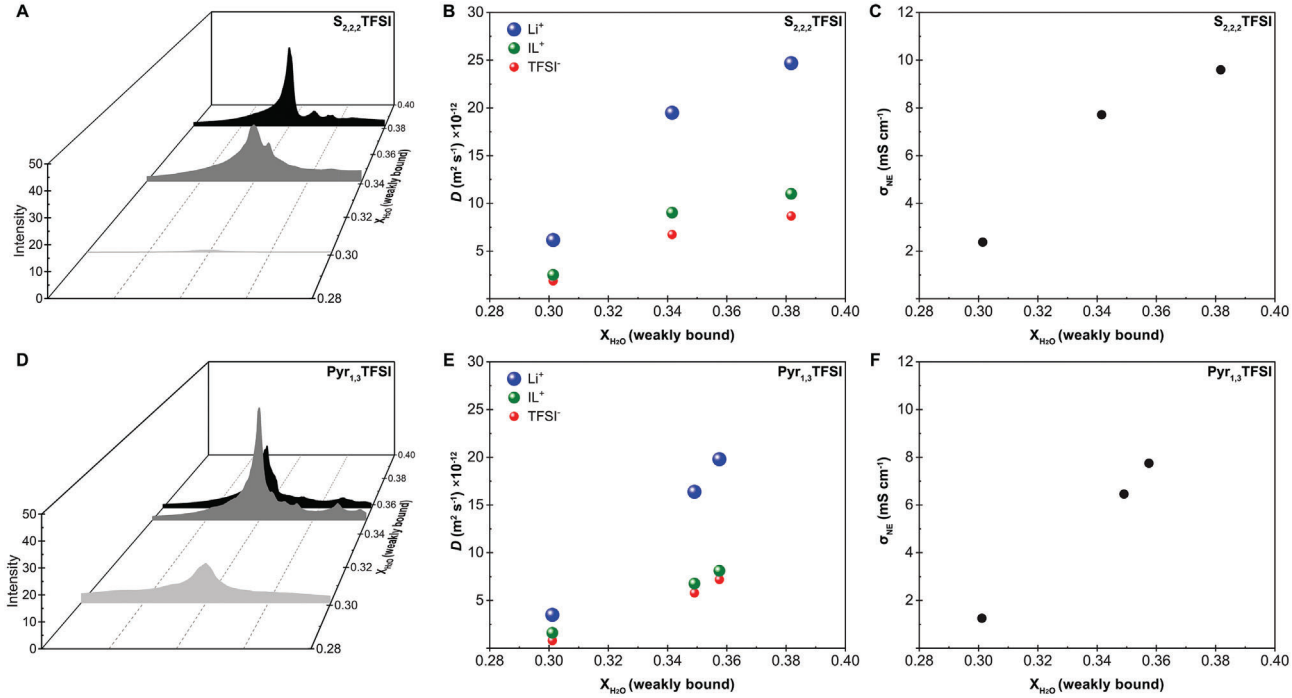

Figure 5. Lineshape analysis (LSA) of NMR 1, 6, and 7 ("group 3"), where only the relative water content was changed, for A–C) $S_{2,2,2}$ and D–F) $Pyr_{1,3}$ HAILSPEs. (A/D) spectral lineshapes of each electrolyte obtained from ^1H NMR measurements. (B/E) and (C/F) calculated ionic diffusion coefficients and conductivity, respectively, as a function of the concentration of weakly bound H_2O in each system, determined by LSA. All electrolyte compositions are given in Tables S4–S7, Supporting Information.

of water is increased, the concentration drops along with the probability of interaction, causing the amplitude and FWHM to slowly align with the completely unbound state, indicating weakly bound H_2O. For the $Pyr_{1,3}$ electrolytes in Figure 5D, the correlations were significantly weaker (0.41, 0.06; Figure S5, Supporting Information). In some cases, this may be due to self-aggregation of the $Pyr_{1,3}$ ionic liquid, which would reduce the degree of water interactions and enhance the frequency of weakly bound water.[30,45] As the self-aggregation process creates slower surfactant-like moieties, this speculation agrees with the measured D_{IL^+} values for $Pyr_{1,3}$ NMR1, 6, and 7, which are 1.33–1.55 times slower than their $S_{2,2,2}$ counterparts.

From the LSA, a quantitative assessment of the amount of strongly bound and weakly bound water in each of the electrolytes was also made based on the relationship between water concentration and FWHM. For each set, boundary conditions were set such that at $X_{H_2O} = 1$ water is entirely in the unbound state and as $X_{H_2O} \to 0$ water is entirely in the bound state. Thus, the amount of bound water in each system was found as a ratio of the sample's FWHM to the FWHM in the completely bound state. The equation of the fit line for the two systems was algebraically rearranged, such that

$$\%H_2O_{bound}\left(S_{2,2,2}\right) = \frac{FWHM\,(ppm) + 2.7}{7.5} \tag{4}$$

and

$$\%H_2O_{bound}\left(Pyr_{1,3}\right) = \frac{FWHM\,(ppm) + 2.0}{5.6} \tag{5}$$

A schematic depicting this process is presented in Figure S6, Supporting Information. Figure 5B,E now shows the diffusion coefficients from Figure 4 as a function of the concentration of strongly bound and weakly bound water. Despite the correlation between water concentration and the spectral lineshape of the $Pyr_{1,3}$ electrolytes being weak, data from $S_{2,2,2}$ and $Pyr_{1,3}$ HAILSPEs show that the increase in ionic mobility is correlated with the amount of water in the weakly bound state. Furthermore, the results suggest that the dramatic increase in diffusion coefficients for $X_{H_2O} > 0.55$, discussed above in Figure 4A,D, may be due to the jump in total weakly bound water that changes the relative viscosity. This trend is translates well to ionic conductivity in Figure 5C,F, which is expected as the Nernst–Einstein (NE) derived values are calculated from the obtained pfg-NMR diffusion coefficients by

$$\sigma_{NE_{25^\circ C}} = \frac{F^2}{RT}\left[c_{LiTFSI}\left(D_{Li^+} + D_{TFSI^-}\right) + c_{IL}\left(D_{IL^+} + D_{TFSI^-}\right)\right] \tag{6}$$

where F is the Faraday constant in units of C mol^{-1}. The values predicted from Equation (6) lie within the range of experimentally determined values discussed above.

2.2. Electrochemical Stability and Passivation

Since PAN is not expected to influence the cathodic limit and the effect of LiTFSI concentration is already well characterized, the impact of water and ionic liquid content on the electrochemical

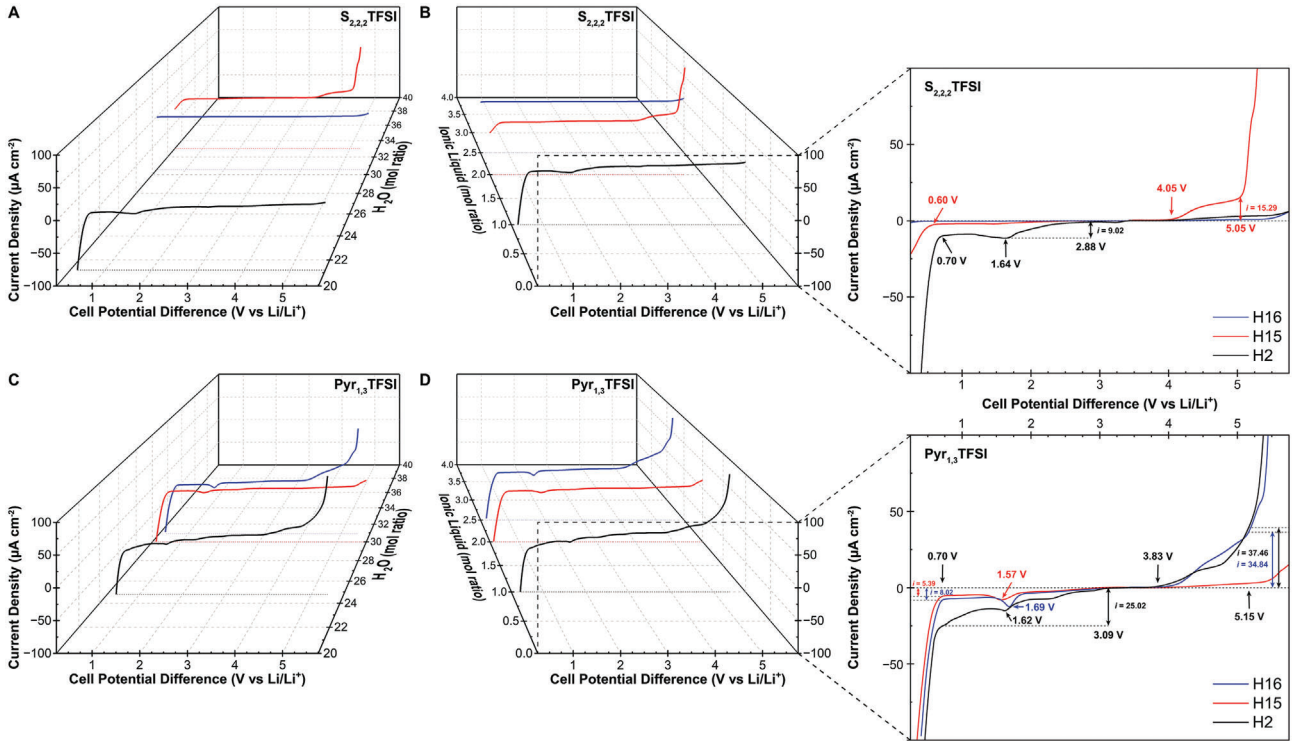

Figure 6. LSV results as a function of H_2O and ionic liquid content for A,B) $S_{2,2,2}$ and C,D) $Pyr_{1,3}$ H2 (black), H15 (green), and H16 (blue) HAILSPE systems measured at room temperature with a scan rate of 0.5 mV s^{-1}. Insets provide a zoomed-in, 2D view of the voltammograms. All electrolyte compositions are given in Tables S8 and S9, Supporting Information.

stability of HAILSPEs and their ability to passivate was investigated. For this reason, three model electrolyte systems – H2, H15, and H16 – were chosen for further exploration (Tables S8 and S9, Supporting Information).

2.2.1. LSV

Figure 6 shows the voltammograms for $S_{2,2,2}$ (A/B) and $Pyr_{1,3}$ (C/D) as a function of both water and ionic liquid content. At the anodic limit >4 V versus Li/Li^+, water and ionic liquid contents do not have an obvious influence, as the onset of electrolyte degradation overlaps for H2 and H16 – which contain different H_2O and ionic liquid contents – in both $S_{2,2,2}$ and $Pyr_{1,3}$ systems. Here, the $S_{2,2,2}$ these electrolytes show only minor oxidation up to 5.5 V versus Li/Li^+, while in the $Pyr_{1,3}$ electrolytes the onset of oxidation is shifted down to 4–5 V versus Li/Li^+ with rapid current evolution at potentials >5 V versus Li/Li^+. The H15 electrolyte exhibited the opposite behavior, with the $Pyr_{1,3}$ system showing greater anodic stability than the $S_{2,2,2}$ system. Nevertheless, for all six HAILSPEs only minor current evolution was observed between 4 and 5 V versus Li/Li^+, followed by complete electrolyte degradation for some systems >5 V versus Li/Li^+. While it can be complicated to precisely determine the ESW in SPEs, these results agree with the generally observed anodic stability of PAN-based SPEs.[46,47] At the cathodic limit, Figure 6 indicates that $S_{2,2,2}$ electrolytes are generally more stable than their $Pyr_{1,3}$ counterparts. This is evidenced by the prominent electrolyte reduction at ≈0.70 V versus Li/Li^+ for all three $Pyr_{1,3}$ HAILSPEs, whereas only one $S_{2,2,2}$ electrolyte (H2) showed reduction at this potential.

2.2.2. CV

To further investigate the LSV results at the cathodic limit, CV was also performed (**Figure 7**) for $S_{2,2,2}$ and $Pyr_{1,3}$, shown in Figure 7A/B,C/D. A modest limit of ≈2 V versus Li/Li^+ was chosen so that the measurements would not cause irreversible electrolyte degradation. From the zoomed-in inset, it is immediately apparent that all three $Pyr_{1,3}$ systems exhibit a greater evolution of current at the cathodic limit than their $S_{2,2,2}$ analogs, regardless of water or ionic liquid content, in agreement with Figure 6. Furthermore, despite $S_{2,2,2}$ and $Pyr_{1,3}$ H2 containing the lowest amount of water (21.20, 24.78), both systems exhibited slower SEI formation that failed to limit H_2O reduction, especially the $Pyr_{1,3}$ electrolyte. Meanwhile, both sets of H15 and H16 electrolytes contained significantly more water (≳30 parts) and exhibited some current evolution on the first cycle, indicating water reduction. However, this response disappeared on the second and subsequent cycles (Figures S7–S12, Supporting Information). This result is also in agreement with Figure 6, which showed that both $S_{2,2,2}$ and $Pyr_{1,3}$ H2 had poor anodic stability compared to H15 and H16; this difference can be attributed to the increase in ionic liquid in the system from 1 part to 2–2.5 parts, which helps to stabilize SEI formation and create a robust, uniform layer.[30,48,49]

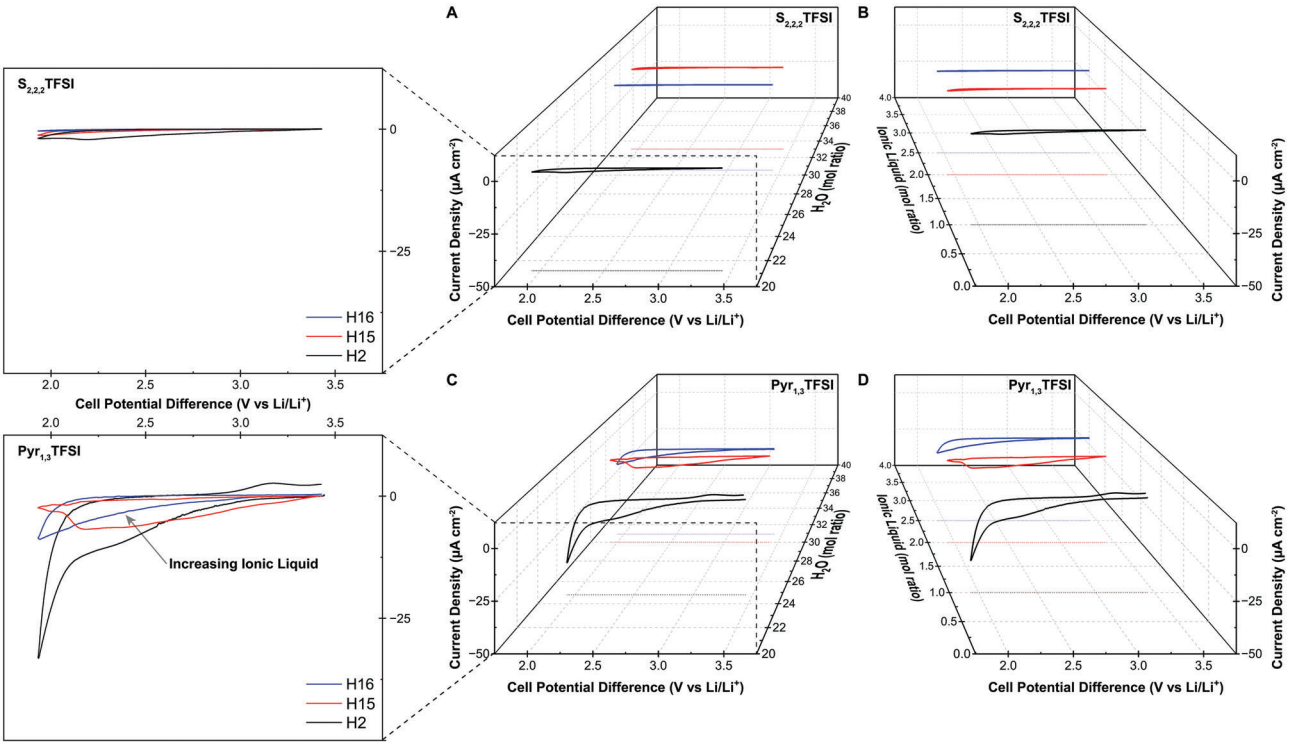

Figure 7. CV results as a function of H_2O and ionic liquid content for A,B) $S_{2,2,2}$ and C,D) $Pyr_{1,3}$ H2 (black), H15 (green), and H16 (blue) HAILSPE systems measured at room temperature with a scan rate of 0.5 mV s^{-1}, limited to 2 V versus Li/Li^+. Insets provide a zoomed-in, 2D view of the voltammograms. Only the first cycle shown; Figures S7–S12, Supporting Information, display the first five cycles for each system. All electrolyte compositions are given in Tables S8 and S9, Supporting Information.

2.2.3. XPS

Figures 6 and 7 suggest that both the choice and amount of ionic liquid in the electrolyte impact the electrochemical stability and passivation behavior of the system. Furthermore, as seen in the zoomed-in insets of Figure 6, a reduction event occurs in both $S_{2,2,2}$ and $Pyr_{1,3}$ electrolytes <2 V versus Li/Li^+ before water reduction and electrolyte degradation. This behavior has also been observed in WiSEs with ionic liquids.[28] Its origin remains unclear, but it may be caused by 1) reduction of $[TFSI]^-$, an essential process in anion-derived SEI formation, or 2) significant generation of hydroxyl groups from the reduction of H_2O, which can nucleophilically attack $[TFSI]^-$ and assist in the anion-derived SEI formation.[50] Due to the lack of sensitivity in the two-electrode configuration using $L_{0.5}FP$, this reduction peak is not always apparent in LSV and CV. Therefore, to further investigate this finding and assess the passivation behavior with greater sensitivity, a three-electrode configuration was necessary. To use the standard Ag/AgCl reference electrode, liquid electrolytes were synthesized sans PAN to circumvent the impracticality of using a fritted reference electrode with the HAILSPEs. These liquid HAILEs were designed with the same H_2O:LiTFSI molar ratio as the HANE, rather than HAILSPEs, to ensure a single-phase system without the solvation power of PAN, but the relative molar amount of the nonaqueous portion – $S_{2,2,2}$ or $Pyr_{1,3}$ – was increased to ensure observation of the reduction of the ionic liquid.[29] The composition of the liquid electrolytes is 1.43 parts H_2O, 2 parts $S_{2,2,2}/Pyr_{1,3}$, and 1 part LiTFSI. Three-electrode CV was conducted with these electrolytes using a Ti foil working electrode and activated carbon counter electrode at a scan rate of 5 mV s^{-1}. Figure S13, Supporting Information shows the first four and 10th cycle from the CV measurements for both HAILEs, where the reduction event <2 V versus Li/Li^+ observed in Figure 6 was reproduced. Furthermore, the CV results of the HAILEs agree with the observations of Figures 6 and 7, which suggested that $S_{2,2,2}$-based electrolytes provided better cathodic stability and passivation than $Pyr_{1,3}$. Therefore, we are confident that the HAILE systems, as designed, are satisfactory analogs for the HAILSPE systems.

To further investigate the passivation behaviors of the $S_{2,2,2}$ and $Pyr_{1,3}$ electrolytes shown in Figure 7, XPS analysis was conducted to determine the chemical compositions of the SEI layers formed by the HAILE analogs, shown in **Figure 8**. Mo_6S_8/HAILE/$LiMn_2O_4$ full cells were cycled 10 times; as seen in Figure 8A–D, both systems observed strong capacity retention and displayed evidence of SEI growth through the jump in coulombic efficiency from ≈92% in the first cycle to ≈97% by the third cycle. Following the final discharge, cells were carefully opened and the cycled Mo_6S_8 electrodes were extracted. The Mo3d spectra (Figure 8E) confirm the presence of SEI formation, as the characteristic Mo(VI) peak, centered ≈232.46 eV, nearly disappeared completely from the pristine anode to the cycled anodes.[51]

The C1s (Figure 8F), F1s (Figure 8G), S2p (Figure 8H), and N1s (Figure 8I) XPS core peaks of the cycled Mo_6S_8 electrodes were analyzed to prove the composition of these SEIs. A summary of the elemental fittings is given in Table S10, Supporting

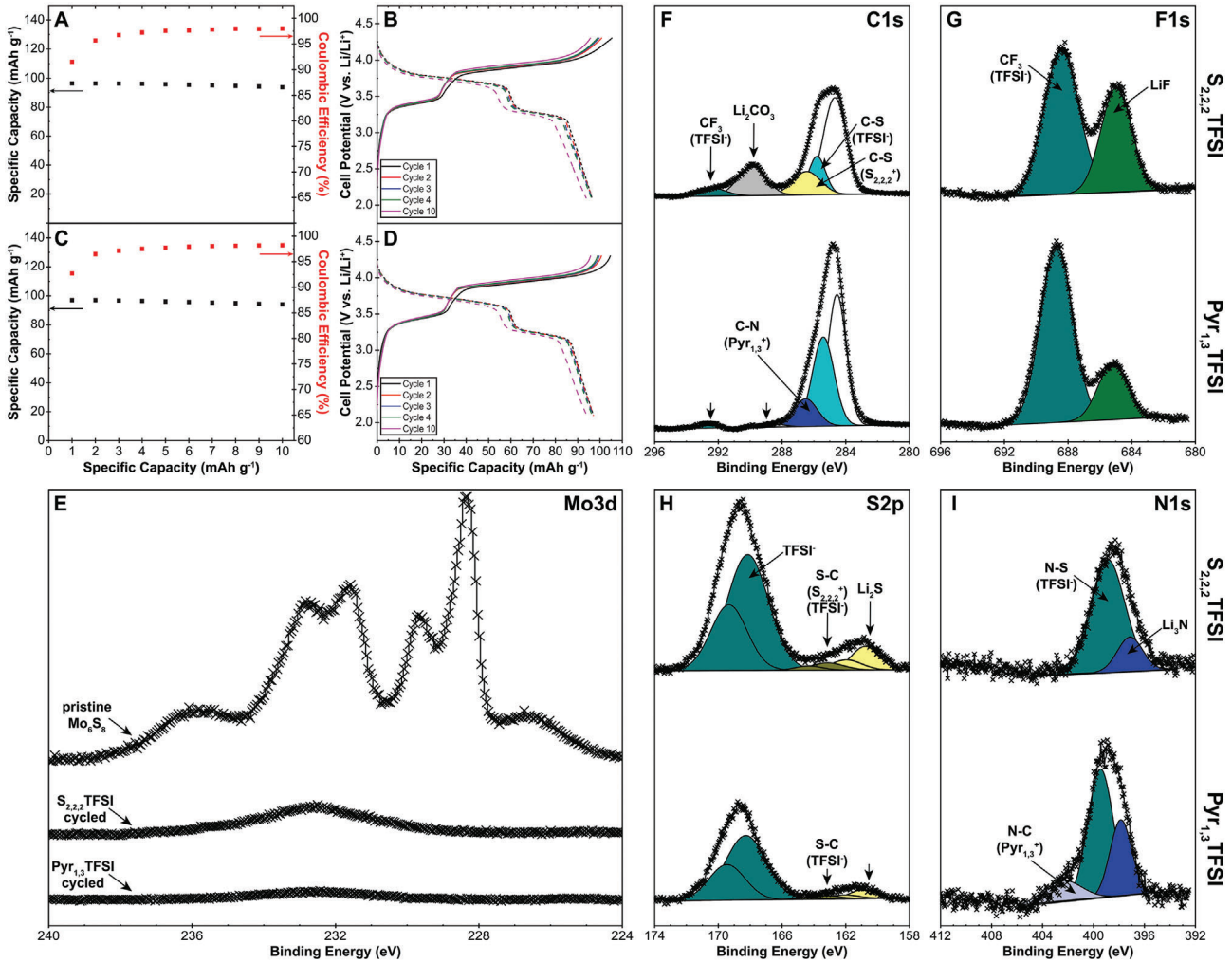

Figure 8. XPS analysis of Mo_6S_8 anodes cycled in $S_{2,2,2}$ and $Pyr_{1,3}$ HAILE electrolytes. A,B) cycling stability and voltage profile of $S_{2,2,2}$ HAILE. C,D) galvanostatic cycling of $Pyr_{1,3}$ HAILE. Spectral data and the relevant fittings are given for I Mo3d, F) C1s, G) F1s, H) S2p, and I) N1s. Cells were cycled at a charge–discharge rate of C/2 at 40 °C for 10 cycles; anodes were then carefully extracted and washed with DMF three times. Specific capacities values are based on the total mass of Mo_6S_8 (11.7 mg cm^{-2}). A summary of the elemental fittings is given in Table S10, Supporting Information.

Information. The large characteristic C1s peak in both spectra is attributed to adventitious hydrocarbons at 284.8 eV; both samples exhibited downward shifts due to static charge, therefore all baselines were corrected.[52] At binding energies >292 eV, the CF_3 peak derives from excess LiTFSI salt on the electrode surface that was not completely washed off, as well as the polyvinylidene (PVdF) binder used in the anode. At lower binding energies <287 eV, the detected signals are attributed to C–S and C–N species derived from $S_{2,2,2}$ and $Pyr_{1,3}$, respectively, as well as the presence of excess LiTFSI.[53] Surprisingly, the C1s in Figure 8F also indicate the formation of Li_2CO_3 as an SEI component in the $S_{2,2,2}$ HAILE. Formation of Li_2CO_3 was unexpected, but may be possible through a two-step reaction pathway: 1) nucleophilic substitution (umpolung) of $S_{2,2,2}$ under alkaline conditions to form ethanol, and 2) oxidation of ethanol into CO_3^-.[54–58] The oxidation of pure ethanol has been observed at potentials of 2.3–2.4 V versus Li/Li^+ in various works, which is within the region of current evolution showed for the $S_{2,2,2}$ HAILE in Figure , Supporting Information.[57,58]

Formation of LiF from the reduction of $[TFSI]^-$, which is contributed by both LiTFSI and ionic liquid, is apparent from the F1s in Figure 8G, which appear at 684.97 and 685.18 eV for $S_{2,2,2}$ and $Pyr_{1,3}$, respectively. Interestingly, the amount of LiF formed in the $S_{2,2,2}$ HAILE is significantly greater than the $Pyr_{1,3}$ electrolyte, which agrees with other studies that show limited LiF growth in $Pyr_{1,3}$-based electrolytes.[53] The residual signal (688.42 and 688.71 eV) can be attributed to excess LiTFSI salt and the PVdF binder. The S2p spectra in Figure 8H indicate the presence of three components. The characteristic peak at 168.15 and 168.28 eV for $S_{2,2,2}$ and $Pyr_{1,3}$, respectively, is categorically assigned to LiTFSI, while the signal at 163.15 and 163.25 eV can be attributed to sulfonyl groups of LiTFSI and $S_{2,2,2}$ (only LiTFSI for the $Pyr_{1,3}$ HAILE).[59] At 160.78 and 160.89 eV, the formation of Li_2S is observed, which can be from the decomposition of both LiTFSI and $S_{2,2,2}$. This is supported by Figure 8H, as the $S_{2,2,2}$ HAILE shows a peak (160.78 eV) with greater intensity than the $Pyr_{1,3}$ HAILE (160.89 eV), suggesting that the ionic liquid further contributes to the formation of Li_2S. Similarly, Figure 8I shows

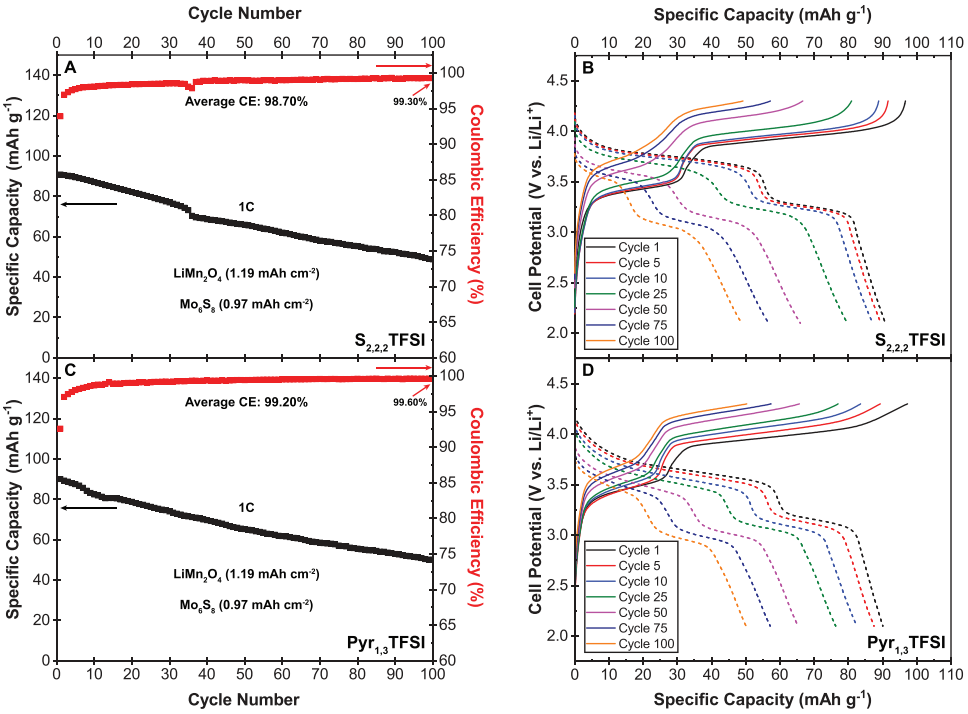

Figure 9. A) Cycling stability and B) voltage profile of $Mo_6S_8/LiMn_2O_4$ full cell with $S_{2,2,2}$ HAILE at a charge–discharge rate of 1 C and 40 °C. C) cycling stability and D) voltage profile of $Mo_6S_8/LiMn_2O_4$ full cell with $Pyr_{1,3}$ HAILE at a charge–discharge rate of 1 C and 40 °C. Specific capacities values are based on the total mass of Mo_6S_8 (11.7 mg cm^{-2}).

that the formation of Li_3N is greater in $Pyr_{1,3}$ HAILE (397.86 eV) compared to $S_{2,2,2}$ HAILE (397.18 eV), which is due to the additional decomposition of the ionic liquid along with the decomposition of LiTFSI.[59] Figure 8I also shows a characteristic signal assigned to the imide groups of LiTFSI and $Pyr_{1,3}$ (only LiTFSI for the $S_{2,2,2}$ HAILE) at 398.93 and 399.46 eV. The residual peak at 402.44 eV in the $Pyr_{1,3}$ HAILE is attributed to the N^+ of $Pyr_{1,3}^+$.[53]

2.2.4. Galvanostatic Cycling

Despite the clear difference in SEI composition and the LSV/CV results suggesting $S_{2,2,2}$ is more stable and better prevents H_2O reduction, the full cell cycling of the $S_{2,2,2}$ and $Pyr_{1,3}$ HAILEs in **Figure 9** show comparable performance over 100 cycles. The electrolytes were cycled in Mo_6S_8 (0.97 mAh cm^{-2})/HAILE/$LiMn_2O_4$ (1.19 mAh cm^{-2}) full cells at a constant charge–discharge rate of 1C at 40 °C. A targeted N:P (negative:positive) capacity ratio of 1:1.3 was used to account for irreversible capacity loss during cycling. $S_{2,2,2}$ shows better capacity retention over the first 25 cycles (87.8%) in Figure 9B compared to $Pyr_{1,3}$ (82.4%) in Figure 9D, but then shows a prominent drop in capacity by cycle 50 to match that of $Pyr_{1,3}$. Nevertheless, both HAILE systems display relatively efficient cycling (99.3%–99.6% CE) up to 100 cycles with clear SEI growth evidenced by the increase in the CE from the first cycle – 93.92% for $S_{2,2,2}$ and 92.60% for $Pyr_{1,3}$ – however, capacity retention decreased to <80% by cycle 35 for both systems. For comparison, the HAILSPE $S_{2,2,2}$ H15 was also cycled in a $Mo_6S_8/LiMn_2O_4$ full cell, and its performance is shown in Figure S14, Supporting Information. Notably, despite the CE (Figure S14A, Supporting Information) and intermittent EIS (Figure S14C, Supporting Information) clearly showing the formation of an SEI within the first 3–5 cycles, the cycling performance and voltage profile (Figure S14B, Supporting Information) display reduced initial capacity utilization (71.4 mAh g^{-1}), slightly reduced average efficiency (98.27% CE), and worse capacity fading over 100 cycles compared to the HAILE analogs. Furthermore, this HAILSPE system was only capable of cycling at a charge–discharge rate of ≈C/30, which is significantly slower than the 1C rate used for the HAILEs. Since $S_{2,2,2}$ H15 showed electrochemical stability beyond 2 V versus Li/Li^+ and minimal water reduction at the lower limit of CV in Figure 7, or significant passivation against H_2O reduction in the case of the HAILEs, a thermodynamic limitation caused by electrolyte degradation is unlikely to be the cause of failure in these systems.[32]

While the exact cause for the cycling behavior observed in Figure 9 and Figure S14, Supporting Information is not fully known, the results indicate poor compatibility between the electrode and electrolytes, likely due to kinetic limitations. This is expected for the HAILSPEs, which is related to the use of porous electrodes tailored for liquid electrolytes that prevent access to available capacity when paired with SPEs. However, because a similar behavior, although not as prominent, is observed in the HAILEs, this behavior may indicate low-quality electrodes. While the intercalation/deintercalation and charge-transfer processes remain efficiently reversible, evidenced by the high coulombic efficiency (>99.30%) after 100 cycles for both liquid and solid systems, the access to usable capacity is being limited with each cycle. This could be due to a reduction in the overall number of lithium redox reactions occurring from the loss of electrical

and/or ionic pathways through the bulk electrode or due to loss of contact at the interface directly. The latter only applies to the solid HAILSPEs, which already suffer from poor interfacial wetting due to the solid nature of the electrolyte. A differential capacity analysis (DCA) of the cycling results from Figure 9 and Figure S14, Supporting Information corroborates this (Supporting Note S1), showing both dQ/dV peak shifting and dQ/dV peak reduction for both HAILE (Figure S15, Supporting Information) and HAILSPE (Figure S14D, Supporting Information) systems. The observation of both peak shifting and reduction with cycling indicates the loss of lithium inventory due to the collapse of both electrical and ionic pathways in the bulk electrode material. This collapse can be caused by processes such as binder decomposition, which decreases particle-particle interactions, and solvent co-intercalation owing to high electrode porosity and/or large pore sizes.[60–63] While the goal of this work was to primarily examine the electrochemical properties of these HAILSPE systems as they relate to transport, electrochemical stability, and passivation, practical performance is a necessary benchmark. The full cell cycling presented herein, while intended to be proof-of-concept, highlights the need for rationally designed and well-fabricated electrodes that can improve the percolation of both ions and electrons to reduce kinetic limitations and electrode failure, assisting in the increased performance of HAILSPEs in full cells.[64]

3. Conclusion

For solid polymer electrolytes (SPEs) to safely meet the demands of high power density and high energy density applications, new design strategies are essential. Contemporaneous improvement of both transport properties and overall electrochemical stability are necessary for this challenge, however these often come alone and seldom together, particularly for aqueous-based SPEs (ASPEs) that add water as a plasticizer. In this work, the in-depth characterization of the composition-function relationships of a new class of ASPEs that includes ionic liquid, coined "hybrid aqueous/ionic liquid" SPEs (HAILSPEs), shines light on an alternative pathway to optimize electrolyte electrochemical stability without sacrificing transport properties. Analysis of HAILSPE transport properties found that the amount of LiTFSI is particularly significant, as its deleterious effect on ionic mobility supersede the benefits of H_2O traditionally seen in ASPEs. However, incorporation of ionic liquid can offset this effect, helping electrolytes achieve with room-temperature ionic conductivity values upward of 8.30 mS cm^{-1} while maintaining Li^+ transport numbers of 0.64–80, depending on the composition. The inclusion of ionic liquid also assists in creating HAILSPE systems with wide ESWs and strong passivation behavior against H_2O reduction. While the work presented here indicates that $S_{2,2,2}$-based HAILSPEs are superior to the $Pyr_{1,3}$-based HAILSPEs, in terms of electrochemical stability and passivation, cycling of $Mo_6S_8/LiMn_2O_4$ full cells with liquid HAIL electrolyte (HAILE) analogs showed similar performance for both systems, likely due to the use of the rather benign Mo_6S_8 anode. Comparison to cycling of the solid HAILSPE demonstrated poorer performance, which was assigned to kinetic limitations of charge transfer and overall electrode quality; this resulted in forced cycling at low C rate and underutilization of the available capacity with capacity fading over 100 cycles. This challenge can be overcome by focusing on the electrode/electrolyte interface to improve interfacial contact, as well as by focusing on better designed electrodes that fulfill the requirements for compatibility with SPEs.

Ultimately, the results of this work suggest that for HAILSPE systems to continue improving, rational design choices that focus on the composition-function relationships are necessary. For example, the choice of ionic liquid has been shown to be paramount to electrolyte performance in both this work and past work. Despite $Pyr_{1,3}$ and other similar pyrrolidinium-based ionic liquids being investigated as electrolyte additives for decades, our work indicates that $S_{2,2,2}$ – a seldomly studied ionic liquid – is superior at passivating against H_2O reduction at the cathodic limit. This example highlights the importance of further tailoring additive chemistry in future iterations of HAILESPEs, including additional novel ionic liquid chemistries that have not been investigated.

Supporting Information

Supporting Information is available from the Wiley Online Library or from the author.

Acknowledgements

This work was supported by the National Science Foundation [grant number CBET2037835]; and the DEVCOM Army Research Laboratory [cooperative agreement number W911NF-22-2-0021]. The opinions, findings, views, conclusions, or recommendations expressed in this material are those of the authors and should not be interpreted as representing the official policies, either expressed or implied, of the Army Research Office, the National Science Foundation, or the U.S. Government. The U.S. Government is authorized to reproduce and distribute reprints for Government purposes notwithstanding any copyright notation herein. The authors are grateful for the US Army Research Laboratory and the Battery Science Branch for use of their facilities and their continued spirit of governmental and academic collaboration. The authors thank Jesse Matthews, Olivier Izmery, and Sam Chen for their early efforts on this work and Jacob Sandler for his efforts on the EIS analysis.

Conflict of Interest

The authors declare no conflict of interest.

Data Availability Statement

The data that support the findings of this study are available from the corresponding author upon reasonable request.

Keywords

all-solid-state batteries, aqueous electrolytes, ionic liquid electrolytes, lithium-ion batteries, solid polymer electrolytes

Received: May 10, 2023
Revised: June 19, 2023
Published online:

[1] J. B. Goodenough, K.-S. Park, *J. Am. Chem. Soc.* **2013**, *135*, 1167.
[2] M. V. Reddy, A. Mauger, C. M. Julien, A. Paolella, K. Zaghib, *Materials* **2020**, *13*, 1884.
[3] P. Albertus, S. Babinec, S. Litzelman, A. Newman, *Nat. Energy* **2017**, *3*, 16.
[4] O. Schmidt, A. Hawkes, A. Gambhir, I. Staffell, *Nat. Energy* **2017**, *2*, 17110.
[5] B. Nykvist, M. Nilsson, *Nat. Clim. Change* **2015**, *5*, 329.
[6] M. J. Lain, J. Brandon, E. Kendrick, *Batteries* **2019**, *5*, 64.
[7] B. Dunn, H. Kamath, J.-M. Tarascon, *Science* **2011**, *334*, 928.
[8] M. Li, J. Lu, Z. Chen, K. Amine, *Adv. Mater.* **2018**, *30*, 1800561.
[9] M. Armand, J.-M. Tarascon, *Nature* **2008**, *451*, 652.
[10] J. B. Goodenough, Y. Kim, *Chem. Mater.* **2010**, *22*, 587.
[11] Y. Lu, C. Z. Zhao, H. Yuan, X. B. Cheng, J. Q. Huang, Q. Zhang, *Adv. Funct. Mater.* **2021**, *31*, 2009925.
[12] M. Osiak, H. Geaney, E. Armstrong, C. O'Dwyer, *J. Mater. Chem. A* **2014**, *2*, 9433.
[13] Q. Wang, L. Jiang, Y. Yu, J. Sun, *Nano Energy* **2019**, *55*, 93.
[14] Q. Zhao, S. Stalin, C.-Z. Zhao, L. A. Archer, *Nat. Rev. Mater.* **2020**, *5*, 229.
[15] J. L. Schaefer, D. A. Yanga, L. A. Archer, *Chem. Mater.* **2013**, *25*, 834.
[16] J. Shin, W. Henderson, S. Passerini, *Electrochem. Commun.* **2003**, *5*, 1016.
[17] M. D. Widstrom, O. Borodin, K. B. Ludwig, J. E. Matthews, S. Bhattacharyya, M. Garaga, A. V. Cresce, A. Jarry, M. Erdi, C. Wang, S. Greenbaum, P. Kofinas, *Macromolecules* **2021**, *54*, 2882.
[18] J.-H. Shin, W. A. Henderson, S. Passerini, *J. Electrochem. Soc.* **2005**, *152*, A978.
[19] J.-H. Shin, W. A. Henderson, G. B. Appetecchi, F. Alessandrini, S. Passerini, *Electrochim. Acta* **2005**, *50*, 3859.
[20] J.-H. Shin, W. A. Henderson, S. Scaccia, P. P. Prosini, S. Passerini, *J. Power Sources* **2006**, *156*, 560.
[21] H. Zhang, X. Liu, H. Li, I. Hasa, S. Passerini, *Angew. Chem., Int. Ed.* **2021**, *60*, 598.
[22] K. Xu, *Chem. Rev.* **2004**, *104*, 4303.
[23] H. Zhang, F. Chen, O. Lakuntza, U. Oteo, L. Qiao, M. Martinez-Ibañez, H. Zhu, J. Carrasco, M. Forsyth, M. Armand, *Angew. Chem., Int. Ed.* **2019**, *58*, 12070.
[24] P. Hu, J. Chai, Y. Duan, Z. Liu, G. Cui, L. Chen, *J. Mater. Chem. A* **2016**, *4*, 10070.
[25] J. Mindemark, M. J. Lacey, T. Bowden, D. Brandell, *Prog. Polym. Sci.* **2018**, *81*, 114.
[26] L. Suo, O. Borodin, T. Gao, M. Olguin, J. Ho, X. Fan, C. Luo, C. Wang, K. Xu, *Science* **2015**, *350*, 938.
[27] L. Suo, O. Borodin, W. Sun, X. Fan, C. Yang, F. Wang, T. Gao, Z. Ma, M. Schroeder, A. von Cresce, S. M. Russell, M. Armand, A. Angell, K. Xu, C. Wang, *Angew. Chem., Int. Ed.* **2016**, *55*, 7136.
[28] A. Tot, L. Zhang, E. J. Berg, P. H. Svensson, L. Kloo, *Sci. Rep.* **2023**, *13*, 2154.
[29] F. Wang, O. Borodin, M. S. Ding, M. Gobet, J. Vatamanu, X. Fan, T. Gao, N. Eidson, Y. Liang, W. Sun, S. Greenbaum, K. Xu, C. Wang, *Joule* **2018**, *2*, 927.
[30] K. B. Ludwig, R. Correll-Brown, M. Freidlin, M. N. Garaga, S. Bhattacharyya, P. M. Gonzales, A. V. Cresce, S. Greenbaum, C. Wang, P. Kofinas, *Electrochim. Acta* **2023**, *453*, 142349.
[31] O. Borodin, L. Suo, M. Gobet, X. Ren, F. Wang, A. Faraone, J. Peng, M. Olguin, M. Schroeder, M. S. Ding, E. Gobrogge, A. von Wald Cresce, S. Munoz, J. A. Dura, S. Greenbaum, C. Wang, K. Xu, *ACS Nano* **2017**, *11*, 10462.
[32] M. D. Widstrom, K. B. Ludwig, J. E. Matthews, A. Jarry, M. Erdi, A. V. Cresce, G. Rubloff, P. Kofinas, *Electrochim. Acta* **2020**, *345*, 136156.
[33] N. Voigt, L. van Wüllen, *Solid State Ion* **2012**, *208*, 8.
[34] M. Watanabe, M. Kanba, K. Nagaoka, I. Shinohara, *J. Polym. Sci.: Polym. Phys. Ed.* **1983**, *21*, 939.
[35] Z. Wang, *Solid State Ion* **1999**, *121*, 141.
[36] B. Wunderlich, *Thermal Analysis of Polymeric Materials*, 1st ed., Springer-Verlag, Berlin/Heidelberg **2005**.
[37] R. Nile, H. Rajput, C. Sims, K. Jin, *Polymer (Guildf)* **2021**, *230*, 124070.
[38] L. Suo, D. Oh, Y. Lin, Z. Zhuo, O. Borodin, T. Gao, F. Wang, A. Kushima, Z. Wang, H.-C. Kim, Y. Qi, W. Yang, F. Pan, J. Li, K. Xu, C. Wang, *J. Am. Chem. Soc.* **2017**, *139*, 18670.
[39] Y. Yamada, A. Yamada, *Chem. Lett.* **2017**, *46*, 1056.
[40] J. Vatamanu, O. Borodin, *J. Phys. Chem. Lett.* **2017**, *8*, 4362.
[41] J. Xu, X. Ji, J. Zhang, C. Yang, P. Wang, S. Liu, K. Ludwig, F. Chen, P. Kofinas, C. Wang, *Nat. Energy* **2022**, *7*, 186.
[42] A. Mittermaier, E. Meneses, in *Protein-Ligand Interactions: Methods and Applications* (Eds: M. A. Williams, T. Daviter), Humana Totowa, NJ **2013**.
[43] A. D. Bain, *Prog. Nucl. Magn. Reson. Spectrosc.* **2003**, *43*, 63.
[44] C. A. Waudby, A. Ramos, L. D. Cabrita, J. Christodoulou, *Sci. Rep.* **2016**, *6*, 24826.
[45] M. Kunze, E. Paillard, S. Jeong, G. B. Appetecchi, M. Schönhoff, M. Winter, S. Passerini, *J. Phys. Chem. C* **2011**, *115*, 19431.
[46] A. Méry, S. Rousselot, D. Lepage, M. Dollé, *Materials* **2021**, *14*, 3840.
[47] D. T. Hallinan, A. Rausch, B. McGill, *Chem. Eng. Sci.* **2016**, *154*, 34.
[48] H.-G. Steinrück, *J. Chem. Phys.* **2021**, *154*, 174703.
[49] I. Bhugun, J.-M. Savéant, *J. Electroanal. Chem.* **1995**, *395*, 127.
[50] N. Dubouis, P. Lemaire, B. Mirvaux, E. Salager, M. Deschamps, A. Grimaud, *Energy Environ. Sci.* **2018**, *11*, 3491.
[51] P. Afanasiev, C. Lorentz, *J. Phys. Chem. C* **2019**, *123*, 7486.
[52] J. F. Moulder, W. F. Stickle, P. E. Sobol, K. D. Bomben, *Handbook of X-ray Photoelectron Spectroscopy: A Reference Book of Standard Spectra for Identification and Interpretation of XPS data* (Ed: J. Chastain), Perkin-Elmer Corporation, Eden Prairie **1992**.
[53] N.-W. Li, Y.-X. Yin, J.-Y. Li, C.-H. Zhang, Y.-G. Guo, *Adv. Sci.* **2017**, *4*, 1600400.
[54] D. Kaiser, I. Klose, R. Oost, J. Neuhaus, N. Maulide, *Chem. Rev.* **2019**, *119*, 8701.
[55] S. I. Kozhushkov, M. Alcarazo, *Eur. J. Inorg. Chem.* **2020**, *2020*, 2486.
[56] C. Zhu, B. Lan, R.-L. Wei, C.-N. Wang, Y.-Y. Yang, *ACS Catal.* **2019**, *9*, 4046.
[57] J. R. Varcoe, P. Atanassov, D. R. Dekel, A. M. Herring, M. A. Hickner, P. A. Kohl, A. R. Kucernak, W. E. Mustain, K. Nijmeijer, K. Scott, T. Xu, L. Zhuang, *Energy Environ. Sci.* **2014**, *7*, 3135.
[58] P. Mukherjee, P. S. Roy, S. K. Bhattacharya, *Int. J. Hydrogen Energy* **2015**, *40*, 13357.
[59] B. Sun, C. Xu, J. Mindemark, T. Gustafsson, K. Edström, D. Brandell, *J. Mater. Chem. A* **2015**, *3*, 13994.
[60] M. Dubarry, V. Svoboda, R. Hwu, B. Y. Liaw, *Electrochem. Solid-State Lett.* **2006**, *9*, A454.
[61] M. Dubarry, V. Svoboda, R. Hwu, B. Y. Liaw, *J. Power Sources* **2007**, *165*, 566.
[62] A. J. Smith, J. R. Dahn, *J. Electrochem. Soc.* **2012**, *159*, A290.
[63] A. J. Smith, J. C. Burns, J. R. Dahn, *Electrochem. Solid-State Lett.* **2011**, *14*, A39.
[64] J. H. Kim, J. M. Kim, S. K. Cho, N. Y. Kim, S. Y. Lee, *Nat. Commun.* **2022**, *13*, 2541.